



Change in photocatalytic NO removal mechanisms of ultrathin BiOBr/BiOI via NO_3^- adsorption

Xian Shi^a, Pingquan Wang^{a,*}, Li Wang^b, Yang Bai^a, Haiquan Xie^b, Ying Zhou^a, Liqun Ye^{a,b,*}

^a State Key Laboratory of Oil and Gas Reservoir Geology and Exploitation, School of Oil & Natural Gas Engineering, Southwest Petroleum University, Chengdu 610500, China

^b Engineering Technology Research Center of Henan Province for Solar Catalysis, College of Chemistry and Pharmaceutical Engineering, Nanyang Normal University, Nanyang 473061, China



ARTICLE INFO

Keywords:
 NO removal
 Ultrathin structure
 BiOBr/BiOI
 NO_3^- adsorption
 Photocatalytic mechanism

ABSTRACT

Improved photocatalytic NO removal of photocatalysts requires enhanced carrier photocatalysis for more reactive species generation. Ultrathin structural BiOBr/BiOI (BiOBr/BiOI-U) photocatalyst was in-situ prepared and it showed enhanced photocatalytic efficiency for NO removal. The underlying photocatalytic process is divided into two steps: in the first step, NO_3^- was produced in a nonselective oxidation process. The increased NO_3^- concentration induces NO_3^- adsorption on the surface oxygen vacancies of the photocatalyst in the second step, which changed the surface environment of the ultrathin BiOBr/BiOI photocatalyst. During this process, the nonselective oxidation process turned into a selective oxidation process with NO_2 as the main product. In addition, the main photogenerated reactive oxygen species contributed to NO removal. Furthermore, the photocatalytic mechanism of BiOBr/BiOI-U was explored.

1. Introduction

Currently, global air pollution is the major environmental deterioration. The poor air quality mainly results from pollution with suspended solid particles (PM), nitric oxide (NO), sulfur dioxide (SO_2), volatile organic compounds (VOCs) and other aromatic hydrocarbons [1]. Among these pollutants, nitric oxide (NO) is mainly produced in fossil energy consumption, which can cause acid rain, photochemical smog and other environmental crises. However, the NO concentration in the atmosphere rose sharply in the past few decades due to the rapid development of transportation and industry. Therefore, development and utilization of green and sustainable strategies for NO removal is urgently necessary. Conventional NO removal technologies are physical adsorption, acid absorption, and alkaline absorption [2–5]. These methods are usually complicated, have high costs, and even cause secondary pollution. Recently, photocatalytic technology has been reported as an efficient alternative strategy for the clean and sustainable NO removal [6]. Upon light illumination, the photocatalysts can generate reactive species, such as photogenerated electrons (e^-) and holes (h^+), superoxide (O_2^-), singlet oxygen (${}^1\text{O}_2$) and so on. Through reaction with these photogenerated species, NO can be effectively

removed [7,8].

Bismuth oxyhalide photocatalysts (BiOX , X = Cl, Br, and I), as a new kind of layered oxide semiconductors, have drawn intense attention due to their superior properties under visible light and their potential applications in engineering. In order to further enhance the photocatalytic properties of BiOX s, a series of structurally modified bismuth oxyhalide photocatalysts have been designed and synthesized. Among them, the heterostructural photocatalyst BiOBr/BiOI has been prepared in one pot. The microstructures of heterojunction-containing BiOBr and BiOI with self-similar structures have a considerable influence on their photocatalytic performances [9–13]. The induced carrier separation efficiency and enhanced molecular oxygen activation ability of BiOBr/BiOI have been confirmed in literature [14–17].

In this work, ultrathin BiOBr/BiOI (BiOBr/BiOI-U) photocatalyst with oxygen vacancies was synthesized in situ and applied for NO removal. The ultrathin structure and the surface oxygen vacancies were determined and comprehensively characterized. We observed an enhanced photocatalytic NO removal efficiency for this photocatalyst, and we analyzed the underlying photocatalytic mechanisms of the NO removal. The mechanism change of photocatalytic NO removal via the NO_3^- adsorption by oxygen vacancies was confirmed. To the best of

* Corresponding authors at: State Key Laboratory of Oil and Gas Reservoir Geology and Exploitation, School of Oil & Natural Gas Engineering, Southwest Petroleum University, Chengdu 610500, China. (P. Wang); Engineering Technology Research Center of Henan Province for Solar Catalysis, College of Chemistry and Pharmaceutical Engineering, Nanyang Normal University, Nanyang 473061, China. (L. Ye).

E-mail addresses: baiyang220523@163.com (P. Wang), yeliquny@163.com (L. Ye).

our knowledge, our study presents the first to use ultrathin BiOBr/BiOI photocatalysts with oxygen vacancies for NO removal. However, only rare studies have been reported on the enhancement of the photocatalytic activity of BiOBr/BiOI.

2. Experimental section

2.1. Materials preparation

BiOBr/BiOI-U: 2 mmol of $\text{Bi}(\text{NO}_3)_3 \cdot 5\text{H}_2\text{O}$ and 1 mmol of KI were firstly dissolved in 40 mL 0.1 mol L^{-1} mannitol solution and then a certain amount of PVP K-30 was dissolved. 40 mL glycol solution containing 1 mmol of KBr was added slowly. After being stirred for 30 min, the result solution was transferred into a 100 mL Teflonlined stainless steel autoclave and filled up to 80% of the total volume followed by a hydrothermal treatment at 160 °C for 16 h. After the reaction, the precipitate BiOBr/BiOI-U was collected, and washed with deionized water and ethanol several times and then dried at 60 °C in air.

BiOBr/BiOI: The same method just used distilled water instead of mannitol solution and without adding PVP K-30.

2.2. Characterization

X-ray diffraction (XRD) spectra of the samples operated at room temperature, by a Bruker D8 advance X-ray diffractometer using Cu $\text{K}\alpha$ radiation and 20 scan rate of 6 min $^{-1}$. Diffraction patterns were taken over the 2θ range 5–70°. X-ray photoelectron spectroscopy (XPS) measurements were carried out by Thermo Scientific ESCALAB 250XI X ray Photoelectron Spectrometer (Al Ka, 150 W, C1 s 284.8 eV). UV-vis diffuse reflectance spectra (DRS) were obtained using UV-vis spectra (Perkin Elmer, Lambda 650 s, BaSO_4 as a reference). Transmission electron microscopy (TEM) and high-resolution transmission electron microscopy (HRTEM) images were obtained by a JEOL JEM-2100 F (RH) Field Emission Electron Microscope.

2.3. Reactive oxygen species (ROS) quantification experiments

Nitrotetrazolium blue chloride (NBT, 2.5×10^{-5} mol L^{-1} , exhibiting an absorption maximum at 259 nm) and 3,3',5,5'-tetramethylbenzidine (TMB, 0.1 g L^{-1} , exhibiting an absorption maximum at 380 nm) were used to determine the photogenerated amount of $\text{O}_2^{\cdot-}$ and ${}^1\text{O}_2$. NBT (2.5×10^{-5} mol L^{-1} , exhibiting an absorption maximum at 259 nm) and TMB (0.1 g L^{-1} , exhibiting an absorption maximum at 380 nm) were used to determine the amount of photocatalytic $\text{O}_2^{\cdot-}$ and ${}^1\text{O}_2$ generation. 10 mg of photocatalysts were added into 50 mL NBT aqueous and sampling every 10 min; 1 mg of photocatalyst was added 16 mL HAc/NaAc buffer solution (pH = 3.6) and 4 mL distilled water, then 2 mg TMB was added in and sampling every 3 min. Both of them were stirred under a xenon lamp. The production of $\text{O}_2^{\cdot-}$ was quantitatively analyzed by detecting the concentration of NBT and ${}^1\text{O}_2$ was analyzed by the oxidation rate of TMB with a UV-vis spectrophotometer.

2.4. ESR tests

50 μL of aqueous suspension of samples (2 mg L^{-1}) was characterized using a Bruker EMX plus model spectrometer operating at the X-band frequency (9.4 GHz) at room temperature for ${}^1\text{O}_2$, $\text{O}_2^{\cdot-}$ and oxygen vacancies test directly with a xenon lamp (50 W) as the light source.

2.5. Photocatalytic NO removal

The photocatalytic experiments of NO removal at ppb levels were performed at ambient temperature in a continuous flow reactor. The volume of the rectangular reactor, which was made of stainless steel

and covered with quartz glass, was 4.5 L (30 cm × 15 cm × 10 cm [L × W × H]). One sample dish containing the sample film was placed in the middle of the reactor. An Xe lamp ($\lambda > 420$ nm) was used as the visible light source. 0.15 g of photocatalyst was added into 15 mL of H_2O and ultrasonicated for 20 min. The aqueous suspension was then coated onto the glass dish, which was then dried at 60 °C until water was completely removed. NO gas was obtained from a compressed gas cylinder at a concentration of NO with traceable National Institute of Standards and Technology specifications. After adsorption–desorption equilibrium among gases and photocatalysts were achieved, the lamp was turned on. The concentration of NO was continuously measured using a chemiluminescence NO analyzer.

2.6. Photoelectrochemical measurement

Electrochemical impedance spectra (EIS) and transient photocurrent responses of the prepared samples were tested by a CHI660D electrochemical working station (CHI Instruments, Shanghai, China) in a three-electrode quartz cell with Na_2SO_4 (0.1 mol L^{-1}) electrolyte solution. Samples were deposited on a fluorinated-tin-oxide (FTO) conducting glass as the working electrode, Ag/AgCl and Pt were used as the reference and the counter electrodes, respectively.

2.7. Trapping experiments

Trapping experiments for photocatalytic NO removal: for detecting the active species during photocatalytic reactivity, singlet oxygen (${}^1\text{O}_2$), superoxide radical ($\text{O}_2^{\cdot-}$) and electron (e^-) were investigated by adding 2 mmol 2,2,6,6- four methylpiperidine nitrogen oxide (TEMPO, a quencher of ${}^1\text{O}_2$), benzoquinone (BQ, a quencher of $\text{O}_2^{\cdot-}$) and AgNO_3 (a quencher of e^-), respectively.

Trapping experiments for exploration of singlet oxygen generation: ESR for singlet oxygen (${}^1\text{O}_2$) were tested without any quencher, adding 2 m mol TEMPO (a quencher of ${}^1\text{O}_2$) and BQ (a quencher of $\text{O}_2^{\cdot-}$), respectively.

3. Results and discussion

X-ray diffraction (XRD) patterns were firstly used to confirm the characteristic diffraction peaks of the as-prepared samples. As shown in Fig. 1a, the characteristic peaks of BiOBr and BiOI were in agreement with reported values (BiOI: PDF: 01-073-2062; BiOBr: PDF: 01-078-0348) [18,19]. As for the heterostructural photocatalysts, they contained all the characteristic peaks of the constituent monomers, which indicated that the coupling of BiOBr and BiOI was successful. Compared with BiOI, the flattened and broadened diffraction peaks of BiOBr/BiOI-U were one of the characteristic features of this ultrathin photocatalyst [20]. Fig. 1b and c showed the morphologies of the as-prepared samples. BiOBr/BiOI-U exhibited uniform, homogeneous, and the smaller flaky BiOI was coupled with BiOBr nanosheets. In contrast, BiOBr/BiOI formed a larger, massive structure. The heterostructures of these two samples were clearly resolved by HRTEM. Fig. 1d and e showed the enlarged ultrathin structure BiOBr/BiOI-U at b1 and b2. Fig. 1d demonstrated that the interlayer distance of the {110} facets in BiOBr were 0.276 nm. Fig. 1e showed that the distance of the {001} facets of BiOI-U was 0.950 nm, which was larger than the distance of 0.915 nm of standard BiOI sample according to a previous report [21]. Fig. 1f, and g were c1 part of Fig. 1c, revealing BiOBr in BiOBr/BiOI. It also demonstrated that the interlayer distance of the {110} facets in BiOBr were 0.276 nm. Selected area electron diffraction (SAED) patterns (Fig. 1g) showed rectangular diffraction points. The angle between {110} and {200} facets was 45°, and the angle between {110} and {1–10} facets was 90°, which was in agreement with previous reports [22]. Fig. 1h and i were c2 part of Fig. 1c. The distance of the {110} facets of BiOI was 0.284 nm, and (SAED) patterns (Fig. 1i) also showed rectangular diffraction points. The angle between {110} and {200}

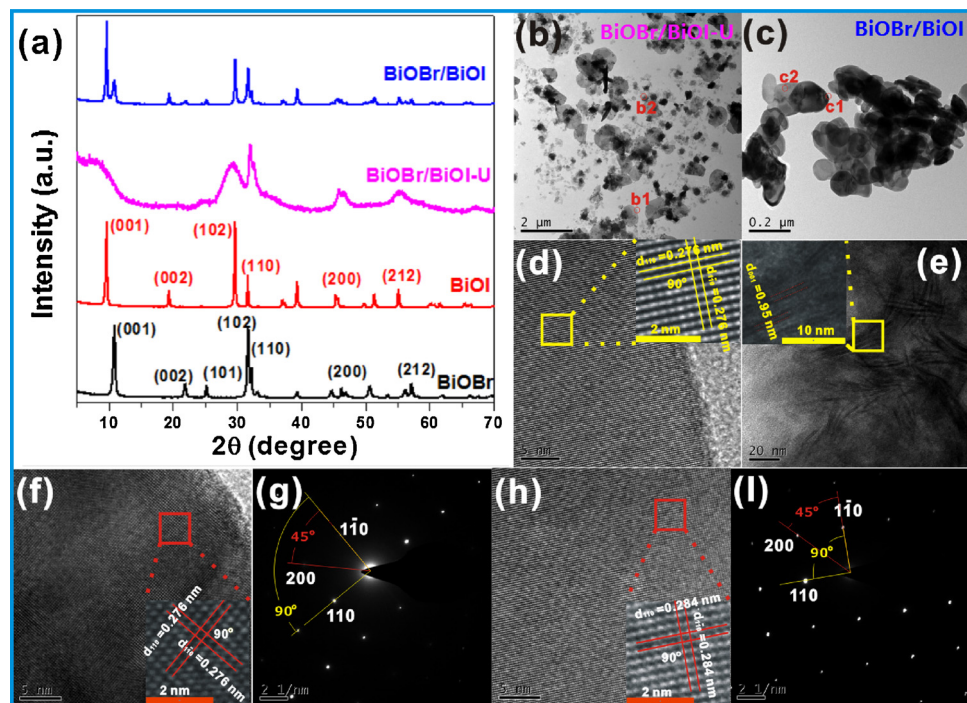


Fig. 1. XRD patterns of BiOBr/BiOI and BiOBr/BiOI-U (a); TEM and HRTEM patterns of BiOBr/BiOI-U (b), (d), (e); TEM and HRTEM patterns of BiOBr/BiOI (c), (f) and (h); and SAED patterns of BiOBr/BiOI (g) and (i).

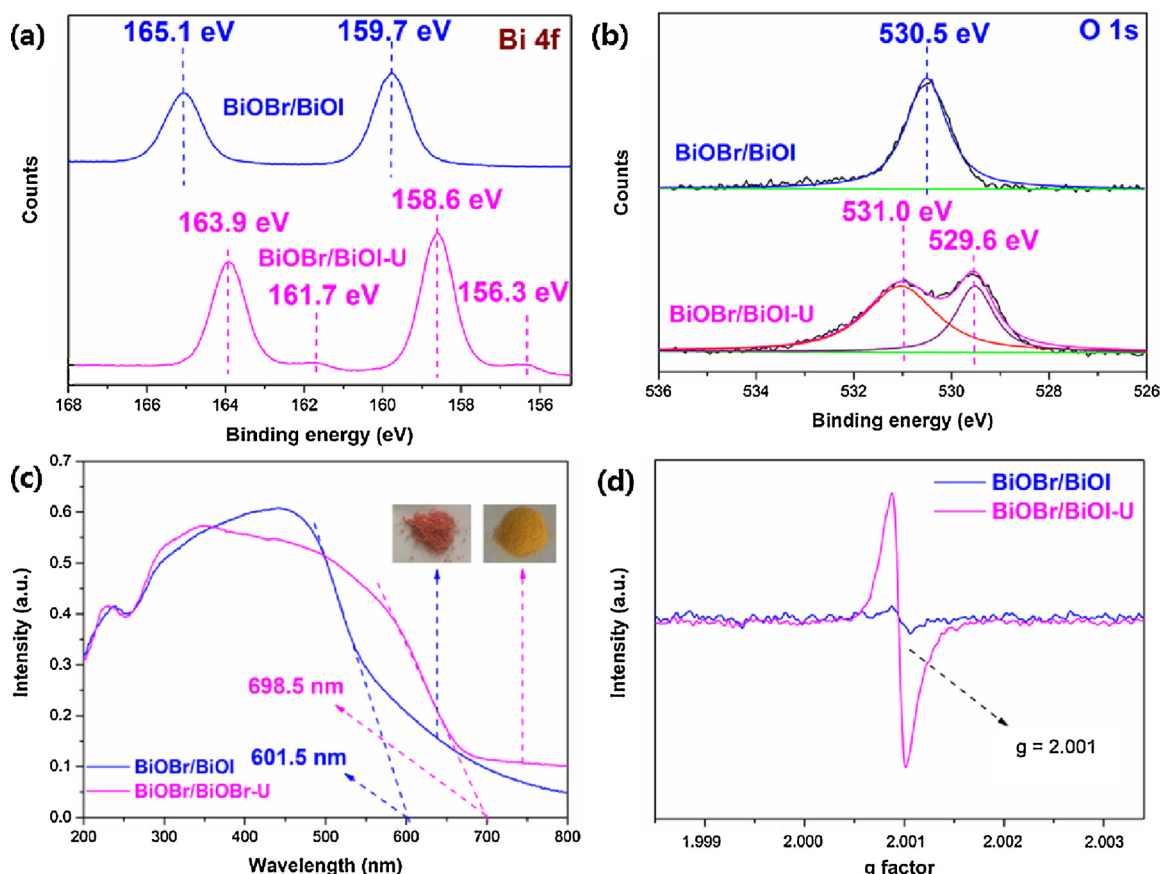


Fig. 2. XPS patterns of Bi 4f (a) and O 1s (b); DRS patterns (c) and EPR (d) of BiOBr/BiOI and BiOBr/BiOI-U.

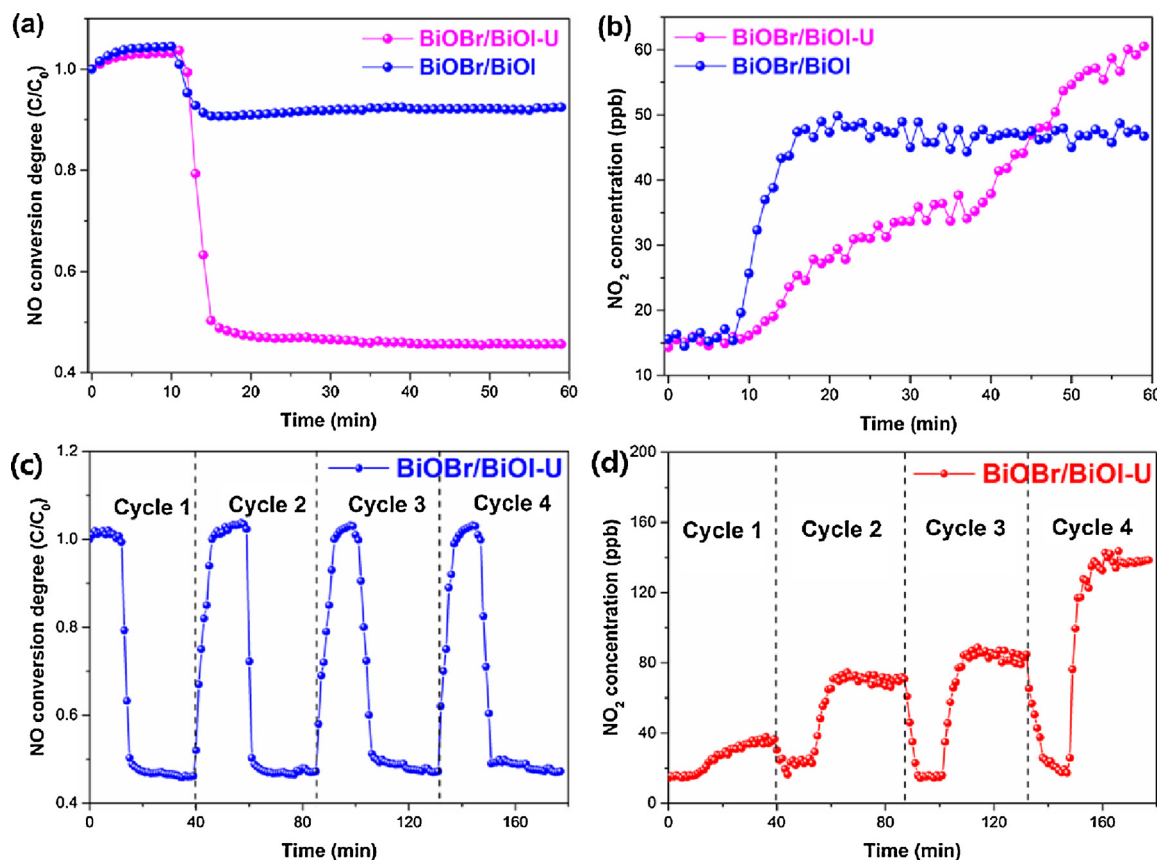


Fig. 3. Comparison of the photocatalytic NO removal of BiOBr/BiOI and BiOBr/BiOI-U (a); NO_2 generation on BiOBr/BiOI and BiOBr/BiOI-U (b); stability of BiOBr/BiOI-U in multiple NO removal cycles (c); and change of the NO_2 concentration with the increasing number of cycles (d).

facets was 45° , and the angle between {110} and {1–10} facets was 90° , which was in agreement with previous reports about BiOI [18,21]. Figure S1 showed the N_2 adsorption and desorption curves of these two samples, which were all type-IV adsorption isotherms [23]. In addition, the hysteresis loops in the adsorption isotherms indicated that BiOBr/BiOI-U and BiOBr/BiOI exhibited mesoporous structures. The specific surface area of BiOBr/BiOI-U was $25.59 \text{ m}^2 \text{ g}^{-1}$, which was larger than the specific surface area of $11.56 \text{ m}^2 \text{ g}^{-1}$ of BiOBr/BiOI. The expanded specific surface area of BiOBr/BiOI-U was caused by its ultrathin structure. The Figure S1 inset showed the pore distribution curves; the peak at 3.54 nm was equaled with the distance between the nanoscales of BiOBr/BiOI-U, which was much narrower than the distance of 25.99 nm determined for BiOBr/BiOI. BET analysis also demonstrated that the enlarged specific surface area of BiOBr/BiOI-U was due to its ultrathin structure.

The elemental compositions of the surfaces were investigated by X-ray photoelectron spectroscopy (XPS; Figure S2a), demonstrating that the surfaces of these two samples consisted of the same elements of Bi, O, Br, and I. Fig. 2a showed that the Bi 4f binding energies of BiOBr/BiOI were values of 165.1 and 159.7 eV . Compared with BiOBr/BiOI, BiOBr/BiOI-U moved toward larger binding energies of 163.9 and 158.6 eV , indicating the appearance of $\text{Bi}^{+(3-x)}$. This phenomenon might be due to the generation of oxygen vacancies according to a previous report, [24] And the oxygen vacancies also supported by the two XPS peaks BiOBr/BiOI-U exhibited at 161.7 and 156.3 eV , which were typical for the formation of oxygen vacancies [21,25]. The O 1s peak at 530.5 eV (Fig. 2b) was assigned to the Bi-O bonds of BiOBr/BiOI. Besides the typical Bi-O bonds at 529.6 eV , BiOBr/BiOI-U showed a peak at 531.0 eV that implied the absence of crystal lattice oxygen [26,27]. Figure S2b and S2c showed the binding energies of BiOBr/BiOI were at 631.1 and 619.6 eV and of BiOBr/BiOI-U were at 630.1 and

618.6 eV , which could be assigned to I 3/2 and I 5/2, respectively. The Br 3d binding energies of BiOBr/BiOI and BiOBr/BiOI-U were at 68.95 and 68.10 eV , respectively. UV-vis diffuse reflectance spectroscopy (DRS) was performed for comparing the maximum absorption wavelength. As shown in Fig. 2c, BiOBr/BiOI-U had a higher visible light absorption than BiOBr/BiOI. This characterization presented an induced property and might be due to the oxygen vacancies according to previous reports [26]. Two pictures inset in Fig. 2c showed that BiOBr/BiOI and BiOBr/BiOI-U were red and dark yellow, respectively. EPR is considered to provide direct evidence of oxygen vacancy formation, and the observed stronger signal implies generation of more oxygen vacancies [28]. In Fig. 2d, both BiOBr/BiOI and BiOBr/BiOI-U showed signals at $g = 2.001$, which were typical for oxygen vacancies [29]. The much stronger signal of BiOBr/BiOI-U indicated that more oxygen vacancies were generated in its bulk structure, which was in agreement with DRS and XPS results.

BiOBr/BiOI-U and BiOBr/BiOI were applied for photocatalytic NO removal in air. Before visible light irradiation, adsorption/desorption equilibrium between gas and samples was reached. After 10 min adsorption, NO removal was initiated on the photocatalysts. Fig. 3a showed changes in the NO concentration (C/C_0) after visible light irradiation for 50 min in the presence of BiOBr/BiOI-U or BiOBr/BiOI. After visible light irradiation of BiOBr/BiOI-U and BiOBr/BiOI was started, the NO concentration started to decrease. We observed that the NO concentration decrease was stronger expressed on BiOBr/BiOI-U than on BiOBr/BiOI. This conclusion was drawn as BiOBr/BiOI-U efficiently removed about 57% of NO by decreasing the concentration from around 600 ppb ($C/C_0 = 1$) to around 258 ppb ($C/C_0 = 0.43$), while BiOBr/BiOI removed only about 10% of NO in 50 min. These outstanding NO removal properties of BiOBr/BiOI-U were due to enhanced carrier photocatalysis, which was also verified by molecular oxygen

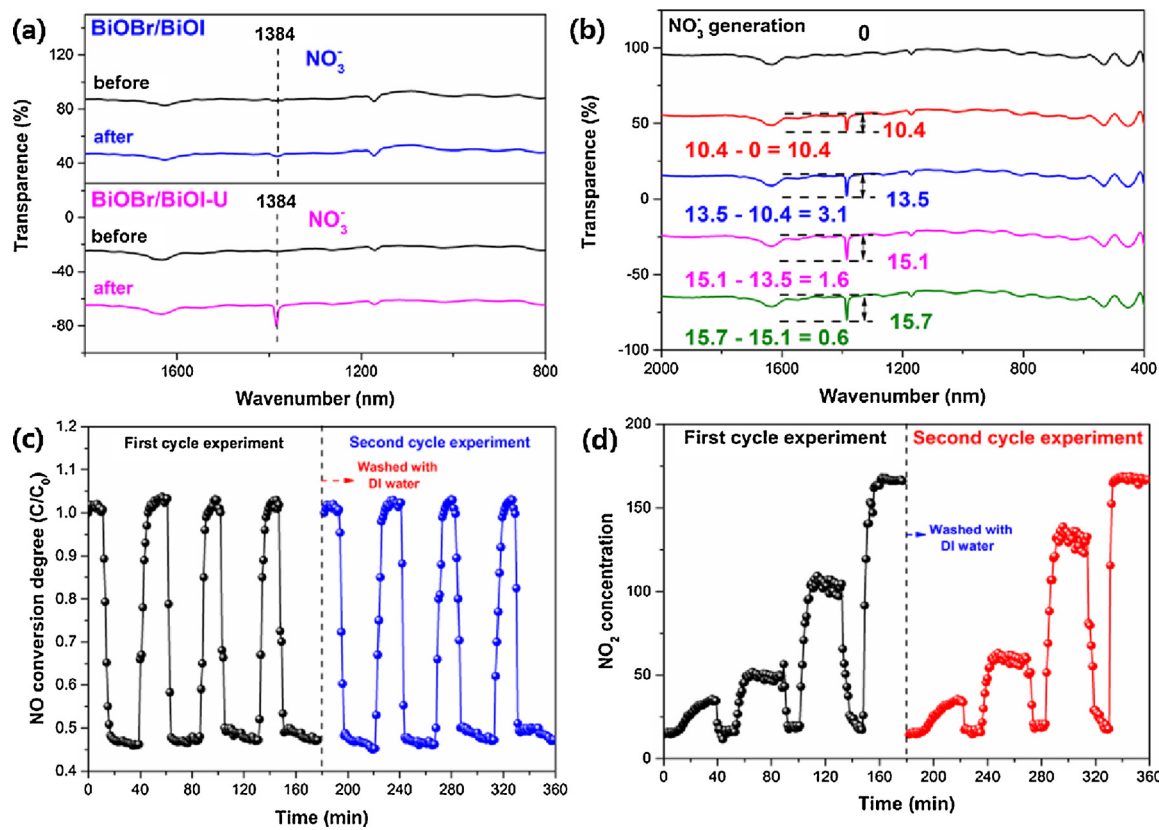


Fig. 4. Original FT-IR patterns (a) and FT-IR patterns after each cycle (b) of BiOBr/BiOI-U; stability of BiOBr/BiOI-U in multiple NO removal cycles before and after washing with deionized (DI) water (c); and change of the NO₂ concentration with increasing cycle number before and after washing with DI water (d).

activation ability, [30,31] equivalent series resistance (ESR; Figure S3), photoluminescence (PL; Figure S4), [32] electrochemical impedance spectroscopy (EIS; Figure S5), [33] transient photocurrent responses (TPR; Figure S6), [34] and ESR trapping experiments (Figure S7) [35]. In addition, we also measured the change of the NO₂ concentration during the whole NO removal process (Fig. 3b). For BiOBr/BiOI-U, we observed that a small amount of NO₂ was produced in the beginning of the NO removal process. This phenomenon demonstrated that NO oxidation induced by BiOBr/BiOI-U was nonselective, and most NO was oxidized to NO₃⁻ [36]. With increasing time, the concentration of NO₂ produced by BiOBr/BiOI-U increased sharply, while that produced by BiOBr/BiOI remained constant. Otherwise, to test the stability of BiOBr/BiOI-U for NO removal, we reused the BiOBr/BiOI-U photocatalyst for four cycles under the same experimental conditions, as shown in Fig. 3c. The photocatalytic NO removal efficiency of BiOBr/BiOI-U did not decline during these four cycles, indicating that BiOBr/BiOI-U was stable and sustainable in the photocatalytic removal of NO. However, Fig. 3d showed that the amount of generated NO₂ increased after each cycle. According to previous reports, [37] NO₃⁻ was expected to be the final product of the nonselective oxidation of the NO removal process, while NO₂ was expected to be the product of the corresponding selective oxidation process. [38] The increased NO₂ concentration (Fig. 3b,d) implied that the nonselective oxidation process might be changed into the selective oxidation process.

In order to further confirm the superior NO removal efficiency of BiOBr/BiOI-U, the amount of produced NO₃⁻ was detected by Fourier transform infrared spectroscopy (FT-IR; Fig. 4a). The peak at 1384 nm was the typical NO₃⁻ signal, [39,40] and we found that its intensity was stronger on BiOBr/BiOI-U than on BiOBr/BiOI, which was in agreement with the NO removal results. To analyze the reason for the change from nonselective to selective oxidation process, we first compared the XRD patterns (Figure S8) of original and used BiOBr/BiOI-U (after four

cycles), which did not show any obvious changes in the crystalline structure of BiOBr/BiOI-U. This finding confirmed that the change in the NO removal mechanism was not accompanied by any structural changes of BiOBr/BiOI-U. In order to confirm that NO₃⁻ was generated in the nonselective oxidation process and influenced the photocatalytic NO removal, the produced NO₃⁻ was measured by FT-IR after each cycle. Although the NO₃⁻ concentration continuously increased, the concentration increment became clearly smaller after each cycle, which was from 10.4 of the 1st cycle to 3.1 of the 2nd, then to 1.6 of the 3rd cycle and 0.6 of final cycle. The sharp decrease of the NO₃⁻ increment (from 10.4 to 3.1) indicated that ultrathin BiOBr/BiOI-U could adsorb more NO₃⁻. Oxygen vacancies on the bulk of the photocatalysts could enhance the adsorption capacity. Herein, to confirm the specific adsorption of the NO₃⁻, EPR was used to detect signal intensity of the oxygen vacancies before and after cyclic experiments. As was shown in Figure S9, the obvious signal decrease could be explained by the NO₃⁻ adsorption. The weak signal of the oxygen vacancies after the cyclic experiment implied that NO₃⁻ was adsorbed on the oxygen vacancies on the bulk of the BiOBr/BiOI-U. The NO₃⁻ adsorption affected the concentration of oxygen vacancies and changed the photocatalytic mechanism of the NO removal. Above experimental results demonstrated that NO₃⁻ generated in the nonselective oxidation adsorbed on the oxygen vacancies of the BiOBr/BiOI-U and changed the photocatalytic NO removal into a selective oxidation process, which also explained the increased NO₂ concentration. In order to further confirm the influence of NO₃⁻, we entirely washed off NO₃⁻ from the BiOBr/BiOI-U photocatalyst using DI water after four cycles and started a new NO removal cyclic experiment. The photocatalyst remained stable for photocatalytic NO removal under visible light irradiation both before and after washing off NO₃⁻ (Fig. 4c). In contrast, the NO₂ generation increased, which was in agreement with previous results (Fig. 4d). However, when the BiOBr/BiOI-U photocatalyst was washed with DI

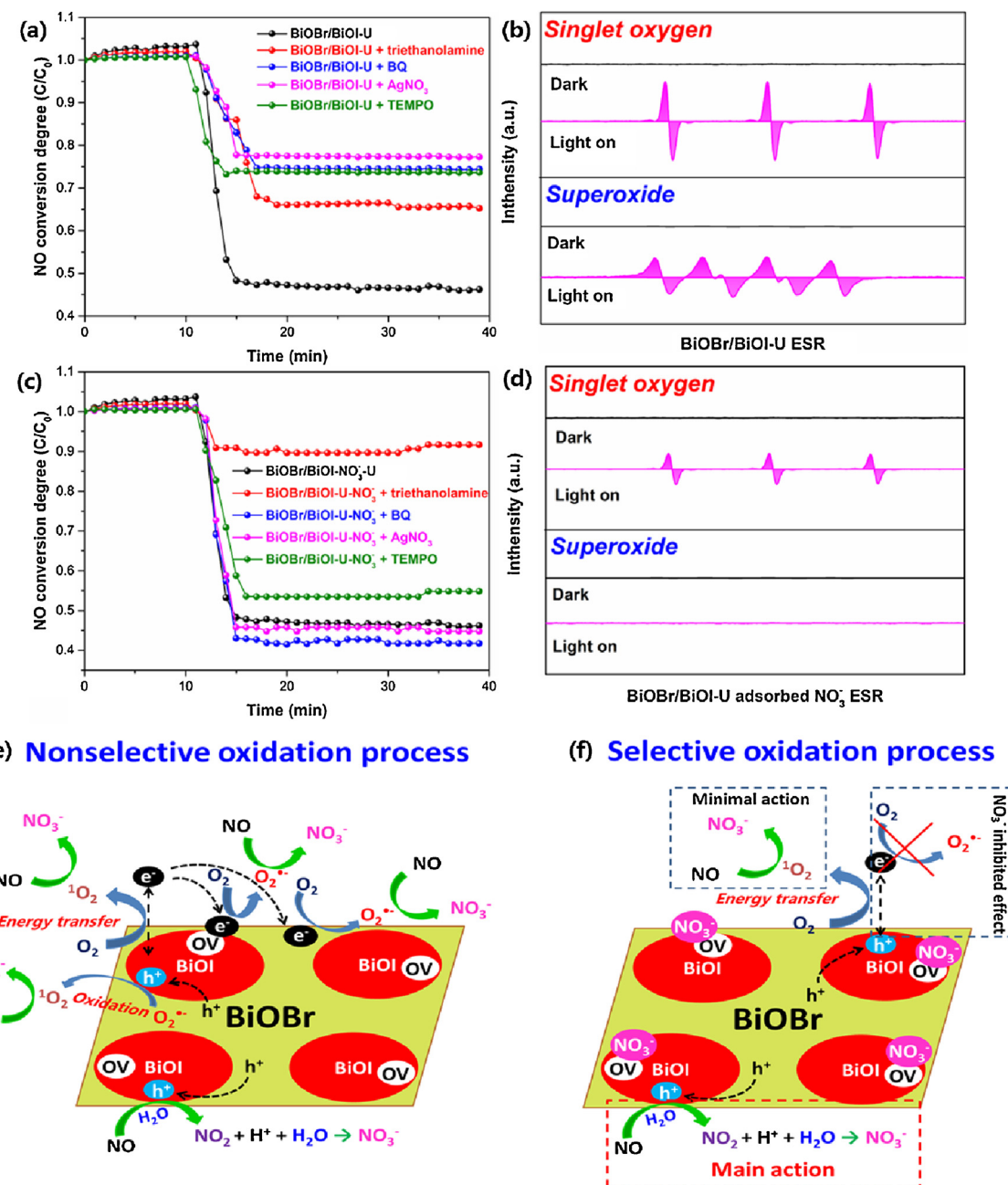
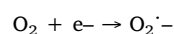
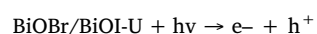


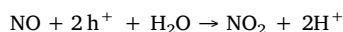
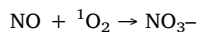
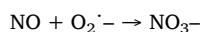
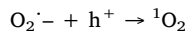
Fig. 5. Comparison of photocatalytic activities of BiOBr/BiOI-U with different trapping agents under visible light irradiation (a); ESR test for $^1\text{O}_2$ and O_2^- in dark and light on (b); comparison of photocatalytic activities of BiOBr/BiOI-U after NO₃⁻ adsorption with different trapping agents under visible light irradiation (c); ESR test for $^1\text{O}_2$ and O_2^- in dark and light on (d). NO removal mechanisms of BiOBr/BiOI-U (e) and (f).

water, the NO₂ amount was notably small and slowly decreased to the original increased amount, which was in agreement with the amount before washing. We concluded that the photocatalytic NO removal process was reverted after NO₃⁻ was washed from the surface oxygen vacancies of the BiOBr/BiOI-U photocatalyst. Therefore, the change of the photocatalytic NO removal process from nonselective to selective oxidation was due to the adsorption of photogenerated NO₃⁻ on the surface oxygen vacancies of BiOBr/BiOI-U.

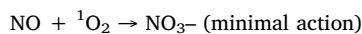
NO removal processes with different trapping agents were studied to elucidate the photocatalytic mechanism. Triethanolamine, benzoquinone, AgNO₃, and tetramethyl piperidine nitrogen oxide (TEMPO) were used for trapping photogenerated holes, O₂^{·-}, electrons, and $^1\text{O}_2$. Fig. 5a showed the trapping results of the nonselective process of the NO removal. Compared with NO removal without any trapping agent, the concentration of NO obviously decreased after adding any of these

trapping agents, indicating that the photogenerated electrons, holes, O₂^{·-}, and $^1\text{O}_2$ were all efficient for NO removal. ESR also proved that BiOBr/BiOI-U effectively generated O₂^{·-} and $^1\text{O}_2$ (Fig. 5b). In combination with previous results, we proposed that photogenerated electrons contribute to the generation of O₂^{·-}. Meanwhile, the oxygen vacancies in the bulk of the BiOBr/BiOI-U photocatalyst were also optimal for O₂^{·-} to capture electrons. $^1\text{O}_2$ was generated by both energy transfer and reaction of O₂ with holes. All these processes promoted the NO removal. In combination with experimental results and previous studies, the nonselective NO removal process could be formulated as follows and illustrated in Fig. 5e: [41,42]





We also explored the photocatalytic mechanism of the NO removal for the BiOBr/BiOI-U photocatalyst after NO_3^- adsorption. Herein, we used the catalyst obtained after the cyclic experiment for the trapping experiments, and the corresponding results were shown in Fig. 5c. After adding benzoquinone and AgNO_3 , BiOBr/BiOI-U remained its original properties for NO removal, suggesting that photogenerated electrons and $\text{O}_2^\cdot -$ did not contribute to the NO removal. While the obvious decline after using triethanolamine and TEMPO indicated that the main reactive species for NO removal were photogenerated holes and ${}^1\text{O}_2$, this mechanism was different from that of BiOBr/BiOI-U before NO_3^- adsorption. According to previous reports, NO_3^- adsorption changed the photocatalyst surface to inhibit the generation of reactive oxygen species. The NO_3^- adsorption cripples the trapped electron capacity of the oxygen vacancies. To confirm this conclusion, we also measured ROSSs of BiOBr/BiOI after NO_3^- adsorption by ESR spectra. No $\text{O}_2^\cdot -$ peaks could be detected in the aqueous dispersions both in dark and light on, confirming that NO_3^- generated during the NO removal process inhibited the generation of $\text{O}_2^\cdot -$, while the weak ${}^1\text{O}_2$ signal proved that ${}^1\text{O}_2$ was only generated by energy transfer rather than reaction of $\text{O}_2^\cdot -$ with holes. Therefore, the presence of oxygen vacancies leaded NO_3^- adsorption, and the photocatalytic mechanisms of NO removal were changed from the nonselective oxidation process into selective oxidation process with a large number of NO_2 generation during this process. The whole process was illustrated in the following and in Fig. 5f: [43,44]



4. Conclusion

In conclusion, the enhanced photocatalytic activity for NO removal of BiOBr/BiOI-U photocatalyst has been showed. Through the XRD, HRTEM and other efficient characterizations, the ultrathin structure and oxygen vacancies of BiOBr/BiOI-U were determined. The mechanism study revealed that the whole photocatalytic NO removal process was divided into two parts: nonselective oxidation process firstly occurred and NO_3^- was the main product in this period. The adsorbed NO_3^- on oxygen vacancies of the BiOBr/BiOI-U changed the photocatalytic NO removal mechanism from nonselective oxidation process to selective oxidation process which induced NO_2 generation. The surface oxygen vacancies of BiOBr/BiOI-U was the key factor for the photocatalytic NO removal mechanism change.

Acknowledgment

This work was supported by the National Natural Science Foundation of China (No. 51872147, 51502146, 51702270, 21671113), the Program for Innovative Research Team of Science and Technology in the University of Henan Province(19IRTSTHN025) and Petro China Innovation Foundation (2018D-5007-0604).

Appendix A. Supplementary data

Supplementary material related to this article can be found, in the online version, at doi:<https://doi.org/10.1016/j.apcatb.2018.10.037>.

References

- [1] Z. Wang, Y. Huang, W. Ho, J. Cao, Z. Shen, S.C. Lee, Fabrication of $\text{Bi}_2\text{O}_3\text{CO}_3/\text{g-C}_3\text{N}_4$ heterojunctions for efficiently photocatalytic NO in air removal: in-situ self-sacrificial synthesis, characterizations and mechanistic study, *Appl. Catal. B Environ.* 199 (2016) 123–133.
- [2] Z. Ai, L. Zhu, S. Lee, L. Zhang, NO treated TiO_2 as an efficient visible light photocatalyst for NO removal, *J. Hazard. Mater.* 192 (2011) 361.
- [3] G. Dong, W. Ho, Y. Li, L. Zhang, Facile synthesis of porous graphene-like carbon nitride ($\text{C}_6\text{N}_6\text{H}_3$) with excellent photocatalytic activity for NO removal, *Appl. Catal. B Environ.* 174 (2015) 477–485.
- [4] J. Luo, G. Dong, Y. Zhu, Z. Yang, C. Wang, Witching of semiconducting behavior from n-type to p-type induced high photocatalytic NO removal activity in $\text{g-C}_3\text{N}_4$, *Appl. Catal. B Environ.* 214 (2017) 46–56.
- [5] C.C. Yu, V.H. Nguyen, J. Lasek, J.C.S. Wu, Titania nanosheet photocatalysts with dominantly exposed (001) reactive facets for photocatalytic NO_x abatement, *Appl. Catal. B Environ.* 219 (2017) 391–400.
- [6] S. Xiao, W. Zhu, P. Liu, F. Liu, W. Dai, D. Zhang, W. Chen, H. Li, CNTs threaded (001) exposed TiO_2 with high activity in photocatalytic NO oxidation, *Nanoscale* 8 (2016) 2899–297.
- [7] W. Cui, J. Li, F. Dong, Y. Sun, G. Jiang, W. Cen, S.C. Lee, Z. Wu, Highly Efficient Performance and conversion pathway of photocatalytic NO oxidation on $\text{SrO}-\text{clusters@amorphous carbon nitride}$, *Environ. Sci. Technol.* 51 (2017) 10682–10690.
- [8] D. Zhang, M. Wen, S. Zhang, P. Liu, Z. Wei, G. Li, H. Li, Au nanoparticles enhanced rutile TiO_2 nanorod bundles with high visible-light photocatalytic performance for NO oxidatio, *Appl. Catal. B Environ.* 147 (2014) 610–616.
- [9] S. Gao, C. Guo, S. Hou, L. Wan, Q. Wang, J. Lv, Y. Zhang, J. Gao, W. Meng, J. Xu, Ionothermal synthesis of hierarchical BiOBr microspheres for water treatment, *J. Hazard. Mater.* 331 (2017) 1–12.
- [10] A. Henríquez, H.D. Mansilla, J. Freer, D. Contreras, Selective oxofunctionalization of cyclohexane over titanium dioxide-based and bismuth oxyhalide (BiOX , $X = \text{Cl}^-$, Br^- , I^-) photocatalysts by visible light irradiation, *Appl. Catal. B Environ.* 206 (2017) 252–262.
- [11] C.Y. Wang, X. Zhang, X.N. Song, W.K. Wang, H.Q. Yu, Novel $\text{Bi}_{12}\text{O}_{15}\text{Cl}_6$ photocatalyst for the degradation of bisphenol a under visible-light irradiation, *Acc Appl. Mater. Interfaces* 8 (2016) 5320–5326.
- [12] X. Shi, X. Chen, X. Chen, S. Zhou, S. Lou, Y. Wang, Y. Lin, PVP assisted hydrothermal synthesis of BiOBr hierarchical nanostructures and high photocatalytic capacity, *Chem. Eng. J.* 222 (2013) 120–127.
- [13] Anirban Dandapat, Hani Gnayema, Yoel Sasso, The fabrication of $\text{BiOCl}_x\text{Br}_{1-x}/\text{alumina}$ composite films with highly exposed (001) facets and their superior photocatalytic activities, *Chem. Commun.* 52 (2016) 2161–2164.
- [14] H. Huang, X. Han, X. Li, S. Wang, P.K. Chu, Y. Zhang, Multiple heterojunctions fabrication with tunable visible-light-active photocatalytic reactivity in the BiOBr-BiOI full range composites based on microstructure modulation and band structures, *Acc Appl. Mater. Interfaces* 7 (2015) 482–492.
- [15] J. Cao, B. Xu, B. Luo, H. Lin, S. Chen, Novel BiOI/BiOBr heterojunction photocatalysts with enhanced visible light photocatalytic properties, *Catal. Commun.* 13 (2011) 63–68.
- [16] J. Cao, B. Xu, H. Lin, B. Luo, S. Chen, Chemical etching preparation of BiOI/BiOBr heterostructures with enhanced photocatalytic properties for organic dye removal, *Chem. Eng. J.* s 185 (2012) 91–99.
- [17] Y. Bai, L. Ye, L. Wang, X. Shi, P. Wang, W. Bai, P.K. Wong, $\text{g-C}_3\text{N}_4/\text{Bi}_2\text{O}_3\text{I}_2$ heterojunction with I^3-/I^- redox mediator for enhanced photocatalytic CO_2 conversion, *Appl. Catal. B Environ.* 194 (2016) 98–104.
- [18] L. Ye, X. Jin, X. Ji, C. Liu, Y. Su, H. Xie, C. Liu, Facet-dependent photocatalytic reduction of CO_2 on BiOI nanosheets, *Chem. Eng. J.* 291 (2016) 39–46.
- [19] D. Zhang, M. Wen, B. Jiang, G. Li, J.C. Yu, Ionothermal synthesis of hierarchical BiOBr microspheres for water treatment, *J. Hazard. Mater.* s 211 (212) (2012) 104–111.
- [20] J. Di, J. Xia, M. Ji, B. Wang, S. Yin, Y. Huang, Z. Chen, H. Li, New insight of Ag quantum dots with the improved molecular oxygen activation ability for photocatalytic applications, *Appl. Catal. B Environ.* 188 (2016) 376–387.
- [21] L. Ye, H. Wang, X. Jin, Y. Su, D. Wang, H. Xie, X. Liu, X. Liu, Synthesis of olive-green few-layered BiOI for efficient photoreduction of CO_2 into solar fuels under visible/near-infrared light, *Sol. Energy Mater. Sol. Cells* 144 (2016) 732–739.
- [22] M. Shang, W.Z. Wang, L. Zhang, Preparation of BiOBr lamellar structure with high photocatalytic activity by CTAB as Br source and template, *J. Hazard. Mater.* 167 (2009) 803–809.
- [23] H. Huang, K. Xiao, Y. He, T. Zhang, F. Dong, X. Du, Y. Zhang, In situ assembly of $\text{BiOI}@\text{Bi}_{1.2}\text{O}_{1.7}\text{Cl}_2$ p-n junction: charge induced unique front-lateral surfaces coupling heterostructure with high exposure of BiOI {001} active facets for robust and nonselective photocatalysis, *Appl. Catal. B Environ.* 199 (2016) 75–86.
- [24] X. Wu, K. Zhang, G. Zhang, S. Yin, Facile preparation of BiOX ($X = \text{Cl}, \text{Br}, \text{I}$) nanoparticles and up-conversion phosphors/BiOBr composites for efficient degradation of NO gas: oxygen vacancy effect and near infrared light responsive mechanism, *Chem. Eng. J.* 325 (2017) 59–70.
- [25] Q. Wang, Z. Liu, D. Liu, G. Liu, M. Yang, F. Cui, W. Wang, Ultrathin two-

- dimensional $\text{BiOBr}_x\text{I}_{1-x}$ solid solution with rich oxygen vacancies for enhanced visible-light-driven photoactivity in environmental remediation, *Appl. Catal. B Environ.* 236 (2018) 222–232.
- [26] J.M. López, A.L. Gilbank, T. García, B. Solsona, S. Agouram, L. Torrente-Murciano, The prevalence of surface oxygen vacancies over the mobility of bulk oxygen in nanostructured ceria for the total toluene oxidation, *Appl. Catal. B Environ.* 174 (175) (2015) 403–412.
- [27] Z. Zhao, Y. Zhou, F. Wang, K. Zhang, S. Yu, K. Cao, Polyaniline-decorated {001} facets of $\text{Bi}_2\text{O}_3\text{CO}_3$ nanosheets: in situ oxygen vacancy formation and enhanced visible light photocatalytic activity, *ACS Appl. Mater. Interfaces* 7 (2015) 730–737.
- [28] A. Moya, A. Cherevan, S. Marchesan, P. Gebhardt, M. Prato, D. Eder, J. Vilatela, Oxygen vacancies and interfaces enhancing photocatalytic hydrogen production in mesoporous CNT/TiO₂ hybrids, *Appl. Catal. B Environ.* 179 (2015) 574–582.
- [29] X. Pan, M.Q. Yang, X. Fu, N. Zhang, Y.J. Xu, Defective TiO₂ with oxygen vacancies: synthesis, properties and photocatalytic applications, *Nanoscale* 5 (2013) 3601–3614.
- [30] Y. Bai, T. Chen, P. Wang, L. Wang, L. Ye, Bismuth-rich $\text{Bi}_4\text{O}_5\text{X}_2$ (X = Br, and I) nanosheets with dominant {1 0 1} facets exposure for photocatalytic H₂ evolution, *Chem. Eng. J.* 304 (2016) 454–460.
- [31] J. Di, J. Xia, H. Li, S. Guo, S. Dai, Bismuth oxyhalide layered materials for energy and environmental applications, *Nano Energy* 41 (2017) 172–192.
- [32] J. Xia, J. Di, H. Li, X. Hui, H. Li, S. Guo, Ionic liquid-induced strategy for carbon quantum dots/BiOX (X = Br, Cl) hybrid nanosheets with superior visible light-driven photocatalysis, *Appl. Catal. B Environ.* 181 (2016) 260–269.
- [33] Z. Zhang, M. Xu, W. Ho, X. Zhang, Z. Yang, X. Wang, Simultaneous excitation of PdCl₂, hybrid mesoporous g-C₃N₄, molecular/solid-state photocatalysts for enhancing the visible-light-induced oxidative removal of nitrogen oxides, *Appl. Catal. B Environ.* 184 (2016) 174–181.
- [34] Y. Zhou, Y. Zhang, M. Lin, J. Long, Z. Zhang, H. Lin, C.S. Jeffrey, X. Wang, Monolayered Bi₂WO₆ nanosheets mimicking heterojunction interface with open surfaces for photocatalysis, *Nat. Commun.* 6 (2015) 8340–8347.
- [35] J. Long, S. Wang, H. Chang, B. Zhao, B. Liu, Y. Zhou, W. Wei, X. Wang, L. Huang, W. Huang, Bi₂MoO₆ nanobelts for crystal facet-enhanced photocatalysis, *Small* 10 (2014) 2791–2795.
- [36] C. Meng, Y. Liu, NO_x removal from vehicle emissions by functionality surface of asphalt road, *J. Hazard. Mater.* 174 (2010) 375–379.
- [37] W. Li, C.Z. Wu, S.H. Zhang, K. Shao, Y. Shi, Evaluation of microbial reduction of Fe (III)EDTA in a chemical absorption-biological reduction integrated NO_x removal system, *Environ. Sci. Technol.* 41 (2007) 639–644.
- [38] F. Xin, W. Zhang, D. Hua, Z. Ni, D. Fan, Y. Zhang, Efficient visible light photocatalytic NO_x removal with cationic Ag clusters-grafted (BiO)₂CO₃ hierarchical superstructures, *J. Hazard. Mater.* 322 (2016) 223–232.
- [39] G. Dong, W. Ho, L. Zhang, Photocatalytic NO removal on BiOI surface: the change from nonselective oxidation to selective oxidation, *Appl. Catal. B Environ.* 168 (169) (2015) 490–496.
- [40] M.A. Gondal, X. Chang, M.A. Ali, Z.H. Yamani, Q. Zhou, G. Ji, Adsorption and degradation performance of Rhodamine B over BiOBr under monochromatic 532 nm pulsed laser exposure, *Appl. Catal. A-Gen.* 397 (2011) 192–200.
- [41] Y. Wang, Y. Huang, W. Ho, L. Zhang, Z. Zou, S. Lee, Biomolecule-controlled hydrothermal synthesis of C-N-S-tridoped TiO₂ nanocrystalline photocatalysts for NO removal under simulated solar light irradiation, *J. Hazard. Mater.* 169 (2009) 77–87.
- [42] K. Hayat, M.A. Gondal, M.M. Khaled, S. Ahmed, A.M. Shemsi, Nano ZnO synthesis by modified sol gel method and its application in heterogeneous photocatalytic removal of phenol from water, *Appl. Catal. A Gen.* 393 (2011) 122–129.
- [43] Z. Ai, S. Lee, Y. Huang, W. Ho, L. Zhang, Photocatalytic removal of NO and HCHO over nanocrystalline Zn₂SnO₄ microcubes for indoor air purification, *J. Hazard. Mater.* 179 (2010) 141–150.
- [44] C. Sun, J. Zhu, Y. Lv, L. Qi, B. Liu, F. Gao, K. Sun, L. Dong, Y. Chen, Dispersion, reduction and catalytic performance of CuO supported on ZrO₂-doped TiO₂ for NO removal by CO, *Appl. Catal. B Environ.* 103 (2011) 206–220.